Fuel 266 (2020) 117030

Contents lists available at ScienceDirect

Fuel

journal homepage: www.elsevier.com/locate/fuel

Full Length Article

Soot primary particle sizing in a n-heptane doped methane/air laminar coflow diffusion flame by planar two-color TiRe-LII and TEM image analysis

F. Patiño[a], J.J. Cruz[a], I. Verdugo[a], J. Morán[b], J.L. Consalvi[c], F. Liu[d], X. Du[e], A. Fuentes[a,*]

[a] Departamento de Industrias, Universidad Técnica Federico Santa María, Av. España 1680, Casilla 110-V, Valparaíso, Chile
[b] Normandie Univ, INSA Rouen, UNIROUEN, CNRS, CORIA, 76000 Rouen, France
[c] Aix-Marseille Université, IUSTI/UMR CNRS 7343, 5 rue E. Fermi, 13453 Marseille Cedex 13, France
[d] Metrology Research Centre, National Research Council of Canada, Ottawa, Ontario, Canada
[e] Energy, Mining and Environment, National Research Council of Canada, Ottawa, Ontario, Canada

ARTICLE INFO

Keywords:
Soot morphology
TEM image analysis
Laminar coflow diffusion flame
Laser induced incandescence
Soot primary particle sizing

ABSTRACT

Soot primary particle size distribution along the centerline of a laminar coflow methane/air diffusion flame doped with vaporized n-heptane at atmospheric pressure was studied using the planar two-color time-resolved laser-induced incandescence (TiRe-LII) technique and analysis of transmission electron microscope images. An improved thermophoretic probe sampling procedure was used to collect samples of soot particles. The LII signals captured at two wavelength bands in the visible are used to determine the soot effective temperature by two-color pyrometry. The methodology was first validated against the literature data obtained in a laminar coflow ethylene/air diffusion flame. The same methodology is then applied to the n-heptane doped methane flame along the flame centerline. The Sauter and geometric mean diameters of soot primary particles were obtained. Good agreement is found between the soot primary particle size distributions obtained by the two techniques.

1. Introduction

The transportation sector is a major contributor to the emissions of greenhouse gases and soot [1]. This sector consumes predominately liquid fuels, especially gasoline and diesel [2]. Due to the inherent complexities of these fuels in compositions, the primary reference fuels (binary mixtures of n-heptane and/or iso-octane) are commonly used as gasoline surrogates for modeling the combustion characteristics of real gasoline [3]. In this context, it is important to understand the sooting characteristics of n-heptane and iso-octane, especially the role of fuel chemistry. Considering the complexity of combustion engines, it is desirable to investigate their sooting characteristics in conventional laminar diffusion flames fueled with vaporized n-heptane or iso-octane to gain a clear understanding of the role of fuel chemistry in soot formation [4]. However, this methodology still encounters the difficulties of flame stability [5,6]. In previous studies, a less sooting gaseous carrier fuel, such as methane, doped with a small amount of PRF fuels [7,8] has been used to study the soot propensity of PRF fuels. In the present work a modified heated Gülder type burner is employed in order to mitigate flame instability issues.

Soot morphological properties such as primary particle diameters are commonly studied based on the thermophoretic sampling (TS) technique and subsequent transmission electron microscopy (TEM) image analysis, despite the uncertainties related to the intrusiveness of this technique. Some attempts, with limited success, have been made to improve the accuracy of soot particle sampling in terms of sampling time and sampling locations. As proposed by Köylü et al. [9], the sampling timing can be monitored by using a specially designed system of laser and a detector to check both the traveling and exposure times. This allows a time resolved verification of the sampling procedure [10]. This objective can also be achieved by using a high-speed camera [11]. However, these methods can be expensive and in fact, as we explain later in the present study, reasonable accuracy can be achieved with a conventional camera by monitoring the attenuated laser signal caused by the sampling grid entering the flame. In addition, the exact sampling location of the TEM grid has usually been overlooked in the literature and there have been no studies monitoring in situ if the sampling grid were placed at the desired location. Here, we present a procedure to determine the sampling grid location to improve the accuracy of the thermophoretic sampling technique.

Several studies have reported the primary particle diameters of soot produced in different liquid fuels particularly focusing on heptane and n-heptane diffusion flames. Qiu et al. [12] and Li et al. [13] have reported the mean primary particle diameters measured at different

* Corresponding author.
E-mail address: andres.fuentes@usm.cl (A. Fuentes).

https://doi.org/10.1016/j.fuel.2020.117030
Received 30 September 2019; Received in revised form 13 December 2019; Accepted 2 January 2020
Available online 13 January 2020
0016-2361/

locations along the centerline for different n-heptane/n-butanol diffusion flames with very low soot volume fractions (< 0.12 *ppm*). Nevertheless, the soot primary particle mean diameters have been found to increase first to reach a maximum value to then decrease monotonically. The reported mean values are within the 10–22 nm range. Botero et al. [14] measured the mean primary particle diameter at the centerline and the wings of a heptane diffusion flame and found no difference in terms of mean values; however, different standard deviations can be inferred from the reported primary particle size distributions. Kashif et al. [4,15] investigated soot formation in laminar methane diffusion flames doped with mixtures of vaporized n-heptane and toluene, finding a monotonically decreasing trend of the soot propensity with increasing the percentage of n-heptane in the fuel mixture. The soot particle size distributions in n-heptane/toluene diffusion flames measured have been reported to be bimodal and the size increases due to toluene addition [16,17]. Typically, the mean primary particle diameters are reported without the corresponding standard deviations. Geometric mean, Sauter diameter and geometric standard deviation are also not commonly reported. Also, for the particular case of n-heptane doped flames of strong interest there has been no attempt to conduct soot primary particle sizing using both the Time Resolved Laser-Induced Incandescence (TiRe-LII) [18] and TEM image analysis. Coupling TEM image analysis with TiRe-LII for primary particle sizing appears a powerful method [19]. The advantages of coupling both techniques are (1) to reduce the measurement uncertainty, since TEM image analysis serves as validation of the TiRe-LII results at limited locations, and (2) to allow imaging of primary particle size distribution in the entire laser sheet with improved accuracy. TEM image analysis is time-consuming and offers only single-point measurement at a small number of locations, while TiRe-LII permits allows rapid measurement of soot primary particle distribution in the excitation laser sheet with high spatial and temporal resolution [20,21].

In this work, the soot primary particle diameter distribution along the centerline of a n-heptane doped methane/air coflow diffusion flame generated using a modified heated Gülder type burner is studied using the methods of TEM image analysis and Ti-Re LII. A brief description of the TiRe-LII model and experimental methodology of combined techniques TiRe-LII and TS sampling/TEM image analysis are given. The two color-pyrometry of flame emission is used to determine the local flame soot temperature. The TS sampling, i.e., the TEM grid, at the flame centerline is ensured by using the line-of-sight attenuation (LOSA) technique. Results of TiRe-LII are compared locally along the flame centerline with the results from TEM image analysis of sampled soot. The sampling of soot was performed following an improved procedure with the help of the LOSA setup to ensure the accurate position of the sampling probe in the flame.

2. Numerical and experimental methodologies

2.1. TiRe-LII model

The TiRe-LII technique uses a short laser pulse (nanosecond scale) to rapidly heat the soot particles to temperatures much higher than the initial state and then detects the resultant spectral incandescence signals (S_{LII}) at different wavelengths in a time-resolved fashion until the soot particles cool significantly [22,23]. As the temperature of larger soot particles decreases slower than that of smaller ones, the interpretation of the signal or soot temperature decay using an appropriate LII model allows the determination of the primary particle size distribution [24,25]. The time-resolved incandescence signals detected at two spectral bands in the visible can be used to infer time-resolved soot effective temperature [22,23,21,26], which in combination with an LII model permits to estimate the Sauter mean diameter (d_{32}) [27] and the geometric mean of the lognormal distribution of soot primary particle diameter [28,29]. The energy equation of a single soot primary particle can be written as [25]:

$$\frac{1}{6}\pi d_s^3 \rho_s c_s \frac{dT}{dt} = C_a F_0 q(t) - \dot{q}_{rad} - \dot{q}_c + \frac{\Delta H_v}{M_v}\frac{dM}{dt}, \tag{1}$$

where d_s is the primary particle diameter, ρ_s and c_s are the soot density and specific heat, respectively. The term C_a is the absorption cross section of the soot primary particle, F_0 is the laser fluence and $q(t)$ is the pulsed laser temporal power density corresponding to unity laser fluence [30]. The term on the LHS of Eq. (1) is the rate of internal energy variation of the single soot particle. The RHS of Eq. (1) represents: the laser energy absorption, the heat loss by thermal radiation, the heat loss by conduction to surrounding gas and the energy loss by soot sublimation. In this work, the soot particle energy loss is modeled considering the processes of conduction [31], radiation [24] (though radiation is negligible at atmospheric pressure), and sublimation losses [32,25]. The sublimation heat loss rate was modeled using the Liu model in [25]. Eq. (1) is solved numerically for a set of soot primary particle diameters ($d_s = [1, 120]$ nm) following the methodology proposed by Liu et al. [27].

Based on the principle of two-color pyrometry, the detected LII signals at the two spectral bands allow to obtain an effective temperature (T_e) of the soot particles, which can be expressed as (here $\lambda_1 < \lambda_2$) [33]:

$$T_e = \frac{hc}{k_B}\left(\frac{1}{\lambda_2} - \frac{1}{\lambda_1}\right)\left[\ln\left(\frac{S_{LII,\lambda_1} E(m_2)\lambda_1^6}{S_{LII,\lambda_2} E(m_1)\lambda_2^6}\right)\right]^{-1}, \tag{2}$$

where $E(m_i)$ is the absorption function dependent on the soot refractive index m_i [34], h is the Planck constant, k_b is the Boltzmann constant and c is the speed of light. On the other hand, the soot effective temperature can also be numerically calculated based on the solutions to Eq. (1) at different primary particle diameters and an assumed size distribution. To this end, the modeled total thermal emission intensity at a wavelength λ_i can be expressed as [28]:

$$TEI_i \propto \int_0^\infty p(d_s)\frac{2\pi c^2 h}{\lambda_i^5}\left[\exp\left(\frac{hc}{\lambda_i k_b T(d_s)}\right) - 1\right]^{-1}\frac{\pi^2 d_s^3 E(m_i)}{\lambda_i}\mathrm{d}(d_s), \tag{3}$$

where, the temperature $T(d_s)$ is the solution of Eq. (1) and $p(d_s)$ is the soot primary particle diameter distribution, which is assumed to follow a lognormal distribution in this work with parameters d_{pg} and σ_g [29]. Similar to Eq. (2) used to determine the experimental effective soot temperature, Eq. (3) allows to determinate the theoretical effective soot temperature based on modeled LII signals at the same two wavelengths as the LII signal detection. Using the Wien's approximation $\exp(hc/k\lambda T) \gg 1$ [33], the theoretical effective soot temperature can be written as

$$T_e = C_2\left(\frac{1}{\lambda_2} - \frac{1}{\lambda_1}\right)/\ln\frac{\int_0^\infty p(d_s) d_s^3 \exp[-C_2/\lambda_1 T(d_s)]\mathrm{d}d_s}{\int_0^\infty p(d_s) d_s^3 \exp[-C_2/\lambda_2 T(d_s)]\mathrm{d}d_s}. \tag{4}$$

Following the method proposed by Liu et al. [27], the primary soot particle diameter distribution parameters d_{pg} and σ_g can be obtained by minimizing the difference between the measured and modeled soot effective temperatures at a moment during particle cooling, i.e, the difference in T_e determined using Eqs. (4) and (2) at a selected time typically about few hundred nanoseconds after the laser pulse, and by using the Sauter mean diameter (d_{32}) determined from the initial decay rate of the experimental soot effective temperature. According to Liu et al. [27], the Sauter mean diameter (d_{32}) can be evaluated based on the initial temperature decay rate in the low-fluence regime (the peak soot temperature is below about 3700 K) as

$$\frac{dT_e}{dt}|_{\tau_{max}} = -\frac{\Theta(T_{max} - T_0)}{d_{32}}, \tag{5}$$

where the peak soot particle temperature (T_{max}) in the low-fluence regime is assumed to be independent of the soot primary particle diameter and the initial soot temperature T_0 (without laser heating) is experimentally obtained by pyrometry. The soot temperature field T_0 is

measured based on spectrally-resolved emission of soot at two wavelengths, according to the methodology developed by Escudero et al. [35]. The parameter Θ represents the thermal properties of soot particles and surrounding gas, necessary to model the heat conduction process, which can be considered in the free-molecular regime in the present study [27]. Finally, for a lognormal distribution the Sauter mean diameter (d_{32}) is related to the two parameters of the lognormal distribution as

$$d_{32} = d_{pg}\exp[2.5(\ln\sigma_g)^2]. \quad (6)$$

For an initial guessed value of σ_g, d_{pg} can be calculated using Eq. (6), where (d_{32}) is obtained from the initial soot effective temperature decay rate determined experimentally. Using these two parameters of the lognormal distribution the theoretical T_e can be determined using Eq. (4). By matching the theoretical effective soot temperature at a selected moment after the laser pulse with that determined experimentally, it is possible to determine the two parameters of the lognormal size distribution as demonstrated by Liu et al. [27].

2.2. Experimental methodology

Fig. 1 displays a schematic of the experimental setup used in this study. The TiRe-LII [20] and TEMs [36] techniques are used directly for soot sizing. Additionally, the LOSA [37] technique is used to monitor the sampling position of the TEM grid to ensure that the TEM grid is stopped at the required sampling position in the flame. In Fig. 1 it is possible to observe some details of the heated burner and the vapor delivery module (VDM) employed to supply the vaporized fuel. In the following section, a brief description is given for each experimental component and diagnostic technique used, more details can be found in the references indicated therein.

2.3. Heated burner and liquid fuel supply

The laminar diffusion flames are generated using a modified heated Gülder type burner (noted by D6 in Fig. 1). A Bronkhorst VDM (D1, model SW-100-2-30-A-21-K) is employed to vaporize n-heptane and mix the vapor with methane (carrier gas). The liquid fuel is stored in a tank (D4) pressurized by an inert gas (N_2) and delivered directly to VDM. To prevent fuel vapor condensation in the burner system, the vaporized fuel/methane mixture is delivered through a Kletti heated hose (D5), controlling the temperature at 130 °C by a KM-RD1002 (D2) and a controller (D8). The vaporized fuel mixture and the co-flow air are both heated and controlled with Omega silicon heater bands (isolated by the burner body D7) to maintain a temperature at 75 °C and 140 °C, respectively. The diffusion flame studied here was fueled with a mixture of vaporized n-heptane with a mass flow rate of 3.27 g/h and methane with a flow rate of 200 cm^3/min. The flow rate of co-flow air was maintained at 90 L/min with a thermal mass flow meter (Bronkhorst SLA5853S2, D3 in Fig. 1).

2.4. TiRe-LII

The set-up for TiRe-LII experiments is presented in Fig. 1 (the C components). The incandescence signal of soot particles (S_{LII}) is produced by the irradiation of a second harmonic (532 nm) Nd:YAG Litron laser pulse model Aurora II (C1) at 10 Hz. A circular aperture of 7 mm diameter selected only the central portion of the beam to produce a nearly top-hat spatial laser profile. The delivered beam energy is attenuated by a combination of half-wave plate and thin-film polarizers. Beam samplers are used to deviate a tiny portion of the laser in order to characterize the energy distributions, both spatially and temporally. The energy is evaluated in a Coherent J-50MB-YAG energy sensor (C4) and Coherent Labmax TOP energy meter (C7). Also, the spatial beam energy distribution is captured at each pulse by a beam profiler Coherent LaserCam-HR II (C3) and a radial average profile of 50 images is shown in the top left inset of Fig. 1. The laser pulse temporal profile is measured by a fast silicon photodetector ET-2030 (C2) of 300 ps rise time, coupled to a digital oscilloscope Tektronix TDS2024C (B5), resulting in a mean pulse duration of 8 ns FWHM at 532 nm. A laser sheet of 200 μm thickness and 70 mm high is generated by the combination of two spherical and one cylindrical lens of $f = -50$ mm, $+100$ mm and -50 mm, respectively. This laser sheet was delivered to pass through the flame centerline. The maximum laser energy deviation is estimated

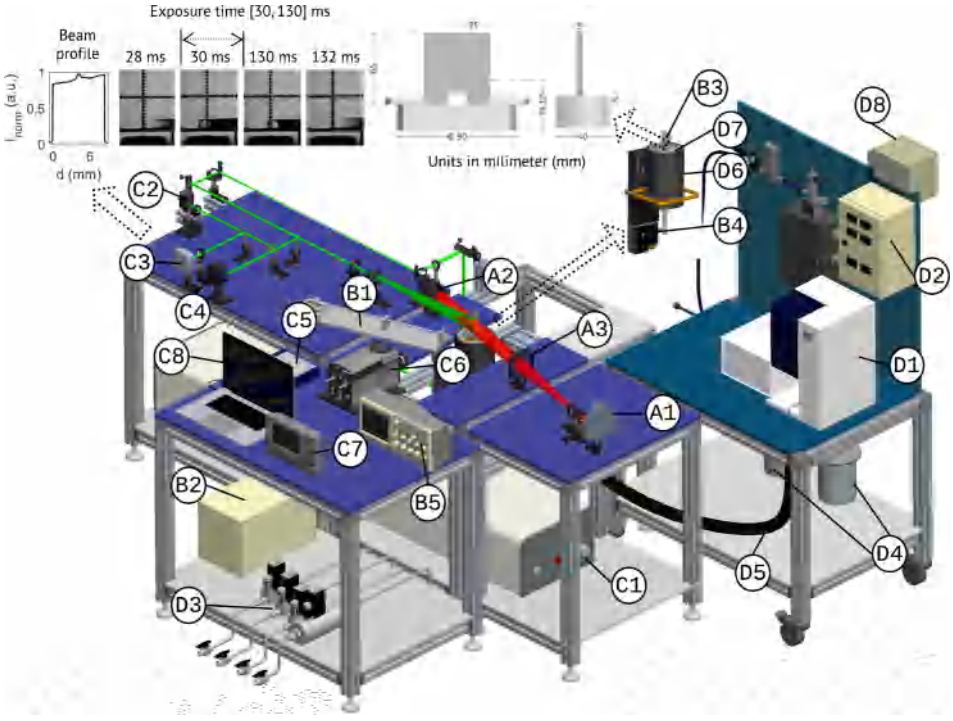

Fig. 1. Schematic of the experimental set-up for the burner system and LOSA, TEM and TiRe LII diagnostics.

Table 1
Thermophoretic sampling conditions.

HAB mm	t_{res} ms	f_v ppm	Zone	HAB mm	t_{res} ms	f_v ppm	Zone
33.7	9.5	0.5	SF	44.1	12.3	1.8	SO
35.7	10.1	1.0	SF	46.1	12.8	1.6	SO
37.8	10.6	1.4	SF	48.2	13.4	1.3	SO
39.9	11.2	1.7	SF	50.3	13.9	0.8	SO
42.0	11.7	1.9		52.4	14.5	0.6	SO

at ~15% from the mean, measured by laser induced fluorescence (LIF) of Rhodamine B [38]. The laser fluence employed in this study was estimated at 0.10 J/cm^2, allowing a good signal-to-noise ratio and to minimize the effect of particle sublimation.

The LII signal S_{LII} is detected at two spectral regions using bandpass filters centered at 450 nm and 650 nm (40 nm bandwidth). This detection is chosen to improve the spectral sensitivity of the detection system and to avoid the interference with the induced PAHs fluorescence [39] and other species [40]. An ICCD camera Andor iStar DH334T (C6) of 1024 × 1024 px coupled with a Nikon AF Nikkor 50 mm lens (f/1.4) is employed to capture the image of LII signals S_{LII}. The detection system is synchronized using an external pulse and delay generator (C5) triggered with the laser Q-Switch. To capture the temporal decay of S_{LII} a set of 150 images are recorded at an interval of 20 ns [20].

The LOSA setup is composed by an ECCD camera (A1), a collimated LED (A2) and an achromatic lens (A3). As explained above, the initial soot temperature before laser heating T_0 is evaluated by two-color pyrometry employing the same set-up devoted to LOSA measurements and following the procedure reported in [35]. As shown in Fig. 1 an Andor Luca R ECCD (A1) camera is employed to capture the soot emissions filtered with bandpass spectral filters (10 nm *FWHM*) centered at 660 nm and 900 nm.

2.5. TEMs particle sizing

Fig. 1 also shows the thermophoretic sampling system (B components) used to collect soot with the rapid insertion of a probe holder, which held a 3 mm diameter, 400 mesh carbon coated copper grid (TED PELLA 01822 and 01844-F). The holder consisting of a 0.37 mm thick and 3.05 mm wide stainless steel tongue was attached to a double acting pneumatic cylinder (B1) electrically controlled by device B2. The methodology to insert the grids inside the flame was adopted according to the procedure proposed by Cortés et al. [36]. A traveling time of ~5 ms (in and out the flame) was verified with a Tektronix TDS 2024C oscilloscope (B5) and was expected to be sufficiently short to avoid soot deposition during the passing of the probe through the flame wing to the flame centerline [41]. A sequence of images were recorded and checked to assure the position of the grid along the flame centerline (see Fig. 1). In the time sequence of images shown at the top of Fig. 1, the grid holder was traveling towards the burner centerline (at 28 ms), reached the centerline (at 30 ms), stopped there between 30 and 130 ms, providing a sample time of 100 ms, and finally returned towards its initial position. Additionally, in this figure it is possible to observe that the holder traveled towards the burner centerline at an axial position just above the burner exit and properly placed as verified by the in situ transparent dimensional calibration grid (B3).

The sampling duration was chosen short enough to cause less than 20% of grid coverage by soot particles according to Dobbins and Megaridis [42] but long enough to collect an adequate amount of particles to ensure that the results of TEM image analysis are statistically meaningful. As reported by Kashif et al. [4], the soot volume fractions (f_v) along the centerline of this flame are fairly low, justifying the fairly long sampling time of this study compared to that typically used in TEM sampling of soot in ethylene diffusion flames (20 to 50 ms). Comparable TEM sampling times can be found in the literature under similar conditions [43,44]. In fact, Kempema et al. [45] tested different sampling times and found no appreciable differences in the resultant primary particle diameters. In addition, the holder position was also verified using the LOSA images. A collected TEM grid would not be analyzed if the holder sampling location was found off the flame centerline. This procedure is particularly important at positions close to the flame tip or when the flame experiences flickering instability. In summary, the TEM sampling system is a prior arranged with the help of the calibration plate along the radial direction and for different height above the burner (HAB) with a linear motor stage (B4). During the experiments, the sample position is also confirmed by taking the images obtained using the LOSA setup (see in Fig. 1), which was adopted to measure the soot volume fraction distribution [37]. In this work, TEM sampling was only performed along the flame centerline. As can be seen in Table 1, f_v along the flame centerline varies between 0.5 and 1.9 ppm over the HAB range considered.

It is noticed that the HAB values in Table 1 refer to those determined by the linear motor stage, but not necessarily the exact locations of the soot particles analyzed from TEM images, given the 3 mm diameter of the sampling grid. Also, in Table 1 HAB = 42 mm is the location where the soot volume fraction peaks and is considered the boundary between soot formation (SF) and soot oxidation (SO) zones for convenience of discussion.

According to the trend of f_v four points were sampled in the SF zone and five points in the SO zone. The corresponding soot residence times (t_{res}) are also reported for each HAB [36]. TEM images were obtained by using a Philips CM30 300 kV transmission electron microscope. These TEM images consist of 1024 × 1024 px and a magnification of 45,000, i.e., the resolution of images is 0.237 nm/px and a maximum length is 242 nm. These images are used to calculate the diameter of primary particles. To this end, there are currently two alternatives available in the literature: automatic, e.g. [46], and manual methods [47,48]. As discussed in [46] both methods provide soot primary particle diameters that are in reasonably good agreement. In fact, the results of the manual method are used to validate those of the automatic method.

3. Results and discussion

3.1. Validation

A set of experimental measurements were first carried out using the same set-up to validate the TiRe-LII technique presented above for soot primary particle sizing. In this case, a laminar diffusion flame generated with 0.22 slpm flowrate of ethylene and 38.2 slpm flow rate of air coflow was employed for the purpose of validation. These experimental conditions are practically the same as those used by Tian et al. [21] and Köylü et al. [9], who applied the TiRe-LII and TEMs techniques, respectively, to determine the geometric mean particle diameter (d_{pg}). As reported by Tian et al. [21], their measurements of S_{LII} were conducted at 400 nm and 450 nm. The S_{LII} decay was recorded until 1000 ns (with an interval of 20 ns) from the laser pulse. An equivalent laser fluence of ~0.19 J/cm^2 was used in the validation procedure, close to the plateau region (~0.22 J/cm^2). Fig. 2 shows the evolution of the fitted normalized LII signals detected at both wavelengths with time. A two-term exponential fit is applied to obtain the decay [49]. Fig. 2 also displays the inferred experimental soot effective temperature (*Te*) obtained in this study (circle symbols) from the ratio of fitted S_{LII} at HAB of 42 mm, at the peak soot volume fraction in the flame. The soot temperatures are compared with the data reported by Tian et al. (diamond symbols), presenting an overall good agreement in terms of the decay rate; however, our soot temperatures are slightly higher. The deviations could be attributed to the small differences in the laser fluence employed and the better accuracy by using a greater wavelength separation in the bandpass filters used [33]. The initial decay rate of the soot effective temperature represents an important property to evaluate the

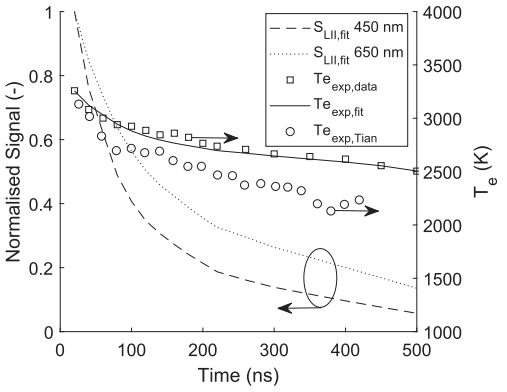

Fig. 2. Time-resolved normalized S_{LII} and effective temperature (T_e).

Table 2
d_{pg} and σ_g for different HAB in the laminar ethylene/air diffusion flame.

Work	HAB mm	d_{pg} nm	σ_g
Köylü et al. [9]	40	25.0	–
This study	40	26.1	1.3
Tian et al. [21]	42	24.0	1.3
This study	42	25.9	1.4

soot primary particle diameter distribution, i.e., d_{32}, d_{pg} and σ_g.

The results obtained at two different HABs, though they are not too far apart, are reported in Table 2, showing an excellent agreement with the TiRe-LII data obtained by Tian et al. [21] and also with the results presented by Köylü et al. [9] from TEM image analysis. Additionally, a sensitivity analysis of the effect of uncertainty in T_0 on the average particle diameter was performed at 40 mm HAB on the flame centerline. The results indicate that a 5% change in T_0 could cause 7% and 8% change in the mean diameter value of d_{32} and d_{pg}, respectively. The deviations could be larger in regions of low soot concentrations, because of the high uncertainties in the soot temperatures, without and with laser heating, derived from the two-color pyrometry.

3.2. Soot particle sizing by TiRe-LII

Once the TiRe-LII procedure for soot particle sizing is validated, the temporal evolution of the LII signals at the same two wavelengths are detected in a laminar coflow methane diffusion flame doped with vaporized n-heptane. Fig. 3 presents the evolution of S_{LII} image captured at the 450 nm band. Each distribution is the result of averaging 150 images captured by the ICCD camera gated at 20 ns with an interval of 20 ns till 1000 ns from the laser pulse. These S_{LII} images were adjusted according to the spatial energy distribution obtained by fluorescence of Rhodamine B, as proposed by Pastor et al. [38]. It is important to indicate that the S_{LII} fields at 650 nm present a similar decay trend. The first image in Fig. 3 shows the field taken at − 20 ns, i.e., the flame emission background. The subsequent LII signal images need to subtract the first background image to eliminate the background flame emission.

To demonstrate the decay of S_{LII}, the LII images at three different time intervals, namely 0–40 ns, 60–200 ns and 300–700 ns, are displayed in Fig. 3. It is clearly shown that S_{LII} increases during the laser pulse and reach the peak intensity at ~20 ns, then starts to decrease monotonically (note that different color scales are used in different time intervals) due to cooling of soot particles. The S_{LII} image intensities are highest at 20 ns, with a peak region located at about HAB ~42 mm. In fact, at this delay time relative to the laser pulse, the S_{LII} image intensity should be proportional to the soot volume fraction (f_v) [23]. This is validated with the results reported by Kashif et al. [4] for the same flame conditions, presenting excellent agreement. These image intensity distributions of S_{LII} at 450 nm and 650 nm are employed to obtain a spatial distribution of d_{32} and d_{pg} following the procedure presented above until the convergence of σ_g. The first step is to define a confidence region where both LII signal intensities captured at 20 ns of delay are above a predefined threshold. The distributions in Fig. 4a show the ratio of the fitted incandescence signals ($S_{LII,\lambda_1}/S_{LII,\lambda_2}$) and the fitted experimental effective temperature ($T_{e,max}$) obtained by two color pyrometry from Eq. (2) at 20 ns. Fig. 4b presents the evolution of the experimental S_{LII} and T_e (symbols) with the fitted signals (dashed lines). It is clear that S_{LII} decreases faster in the first 200 ns, by the cooling of soot particles reducing T_e by about ~500 K. Afterwards T_e decreases slowly and monotonically. A two-term exponential fit is also implemented to the experimental incandescence signals and the ratio of the fitted signals is used to calculated the fitted effective temperature ($T_{e,fit}$) presenting excellent agreement with the two color experimental temperatures. The initial temperature decay (dT_e/dt of Eq. (5)) is calculated from the derivative of the fitted effective temperature ($T_{e,fit}$) between the time of the peak effective temperature (~20 ns) and 100 ns. This gradient allows to evaluate the d_{32} distribution of soot particles shown in Fig. 4c. The obtained values of d_{32} between 15 and 35 nm are somewhat expected. However, some irregular distributions appear around HAB = 48 mm, due to very low signal-to-noise ratios of S_{LII}, leading to erroneous fit of the effective temperature. From this d_{32} field the iterative procedure is carried out to obtain the two parameters of a lognormal distribution, along with the experimental effective soot temperature at a fairly long delay after the laser pulse. The iterative process was stopped when the relative error between the predicted and measured T_e at a delay of 550 ns [27] is less than 10^{-6}. The distribution of geometric mean diameter is presented in Fig. 4c. An average of about $d_{pg} \approx 19$ nm is obtained and most values are in the range of 15–35 nm. Again, similar irregular region for d_{32} appear for d_{pg} distribution for the same reason of very low signal-to-noise ratios.

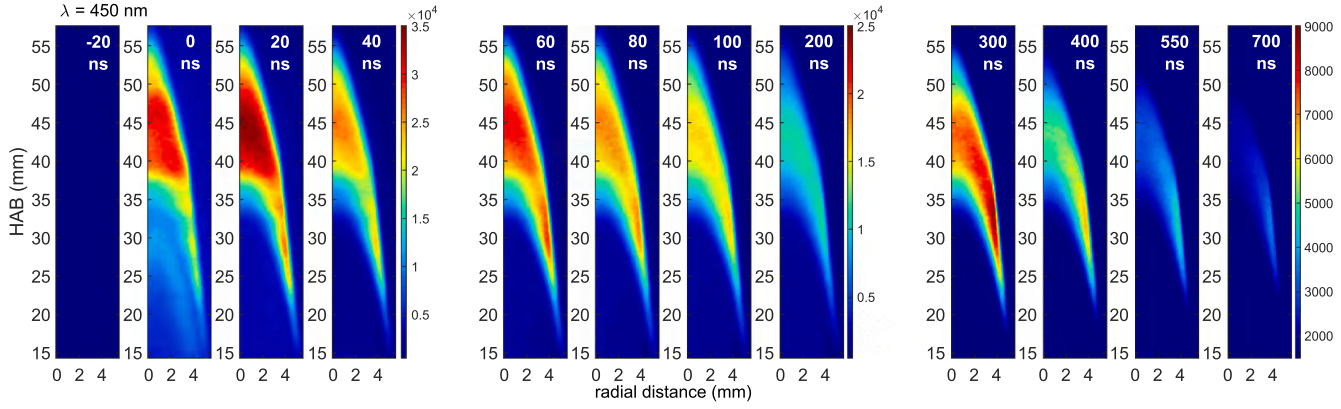

Fig. 3. Temporal evolution of the LII signal at different intervals for 450 nm.

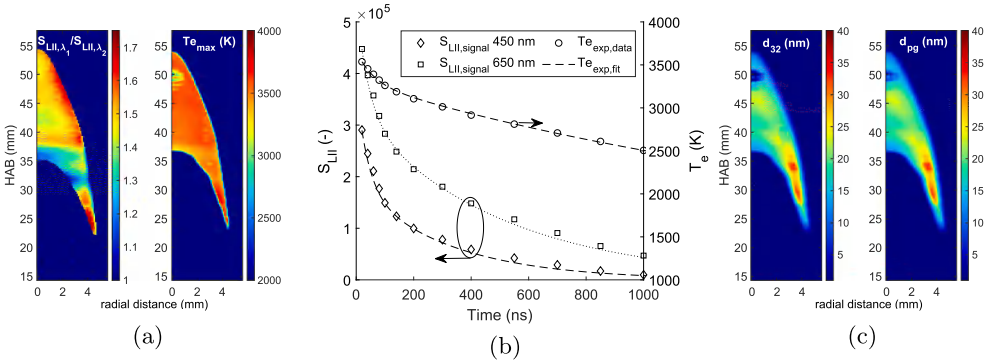

Fig. 4. (a) Fields of the fitted ratio $S_{LII,\lambda_1}/S_{LII,\lambda_2}$ and the peak of the temperature Te_{max}. (b) Time evolution of the S_{LII} and effective temperature (T_e) for $HAB = 30$ mm. (c) Distributions of the Sauter mean and geometric mean.

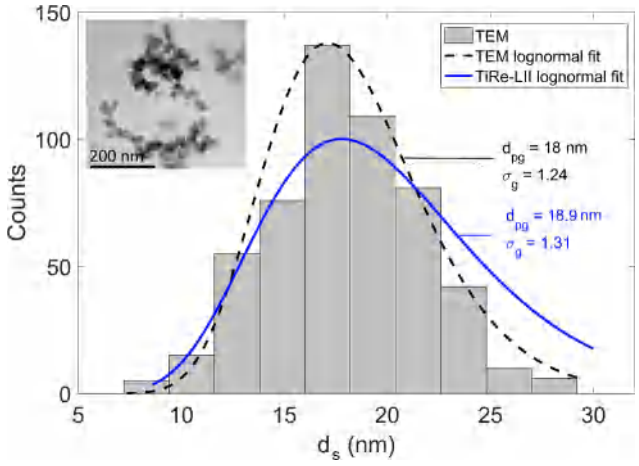

Fig. 5. Comparison of the primary particle diameter distributions obtained by TEMs and TiRe-LII at HAB = 39.9 mm.

3.3. Comparisons the results of TiRe-LII and TEMs

The results of soot primary particle diameter distributions obtained by the TEM image analysis and TiRe-LII techniques are compared in Fig. 5. A typical TEM image of soot particles aggregates obtained by TS at $HAB = 39.9$ mm is presented in the same figure. A satisfactory agreement is noticed between the two lognormal distributions from TEM image analysis and the TiRe-LII method. Similar trends are also observed at other locations along the flame centerline.

Comparison of d_{32} and d_{pg} along the flame centerline was also made and the results are summarized in Table 3, which presents the variation of both mean soot particle diameters at different HABs. In the SF region comparable results and trend are obtained by both techniques, showing that both d_{32} and d_{pg} increase with HAB until HAB = 42 mm. The agreement becomes less satisfactory above the 50 mm of height in the SO region, though the results of d_{32} and d_{pg} from both methods exhibit the same decreasing trend with increasing HAB. Specifically, TiRe-LII provides smaller d_{32} in the SF zone.

As observed in the Table 3 an average discrepancy of 13% and 26% was obtained in the region of flame tip (HAB > 48 mm) for d_{pg} and d_{32}, respectively. We believe that the larger discrepancies in this small part of the flame are mainly attributed to the larger uncertainties in the measured soot temperature, without or with laser heating, due to the low soot volume fractions in regions close to the flame tip.

Table 3
Comparison between TiRe-LII and TEMs for d_{pg} and d_{32} at different HAB.

HAB mm		33.7	35.7	37.8	39.9	42	44.1	46.1	48.2	50.3	52.4
d_{32} nm	TEM	17.3	18.4	22.6	20.0	24.4	18.4	17.6	16.1	15.3	15.9
	TiRe-LII	12.9	15.7	18.6	18.3	22.1	21.5	17.9	15.8	11.3	–
d_{pg} nm	TEM	15.1	16.2	18.3	18.0	20.3	16.4	15.6	13.5	13.4	12.7
	TiRe-LII	12.7	16.4	18.5	18.9	21.4	20.8	17.8	15.7	11.6	–
Zone		SF							SO		

4. Conclusions

In this work, the soot primary particle diameter distribution along the centerline of a vaporized n-heptane doped methane/air laminar coflow diffusion flame was investigated using a planar two-color time-resolved LII technique and by analysis of TEM images of thermophoretically sampled soot particles. The TEM sampling time and grid location were carefully verified by capturing a sequence of images before establishing the flame and during the TEM sampling with the flame by capturing the light-of-sigh attenuation (LOSA) images to ensure the sampling grid was placed at the desired locations. Time-resolved planar LII images were acquired up to 1000 ns from the onset of laser pulse by shifting the delay time of the ICCD camera at an intervals of 20 ns. The methodology to evaluate d_{32} and d_{pg} from TiRe-LII measurements is validated by comparing with the reported data taken in a laminar coflow ethylene/air diffusion flame, using the same setup and data analysis approach. The results of soot primary particle diameter distribution obtained by TEM image analysis and TiRe-LII along the flame centerline are in fairly good agreement, especially in the soot formation zone below the location of the peak soot volume fraction at 42 mm. In the soot formation zone below 42 mm, TiRe-LII measured smaller values of Sauter mean of primary particles than TEM image analysis. Further work is planned to investigate the effects of fuel chemistry on soot primary particle size distribution.

Acknowledgments

This work was partially supported by DGIIP UTFSM through the PIIC initiative, Fondecyt regular project 1191758, CONICYT PIA/ANILLO ACT172095 project and the Fondecyt postdoctoral project 3190860.

References

[1] Kohse-Hoinghaus K. Clean combustion: chemistry and diagnostics for a systems approach in transportation and energy conversion. Prog Energy Combust Sci 2018;65:1–5. https://doi.org/10.1016/j.pecs.2017.10.001.
[2] Demirbas A. Progress and recent trends in biofuels. Prog Energy Combust Sci 2007;33(1):1–18. https://doi.org/10.1016/j.pecs.2006.06.001.
[3] Cai L, Pitsch H. Optimized chemical mechanism for combustion of gasoline surrogate fuels. Combust Flame 2015;162(5):1623–37. https://doi.org/10.1016/j.combustflame.2014.11.018.
[4] Kashif M, Guibert P, Bonnety J, Legros G. Sooting tendencies of primary reference fuels in atmospheric laminar diffusion flames burning into vitiated air. Combust Flame 2014;161(6):1575–86. https://doi.org/10.1016/j.combustflame.2013.12.009.

[5] Khosousi A, Liu F, Dworkin SB, Eaves NA, Thomson MJ, He X, Dai Y, Gao Y, Liu F, Shuai S, et al. Experimental and numerical study of soot formation in laminar co-flow diffusion flames of gasoline/ethanol blends. Combust Flame 2015;162(10):3925–33. https://doi.org/10.1016/j.combustflame.2015.07.029.

[6] Merchan-Merchan W, McCollam S, Pugliese JFC. Soot formation in diffusion oxygen-enhanced biodiesel flames. Fuel 2015;156:129–41. https://doi.org/10.1016/j.fuel.2015.04.011.

[7] Das DD, Cannella WJ, McEnally CS, Mueller CJ, Pfefferle LD. Two-dimensional soot volume fraction measurements in flames doped with large hydrocarbons. Proc Combust Inst 2017;36(1):871–9. https://doi.org/10.1016/j.proci.2016.06.047.

[8] Das DD, John PCS, McEnally CS, Kim S, Pfefferle LD. Measuring and predicting sooting tendencies of oxygenates, alkanes, alkenes, cycloalkanes, and aromatics on a unified scale. Combust Flame 2018;190:349–64. https://doi.org/10.1016/j.combustflame.2017.12.005.

[9] Köylü U, McEnally C, Rosner D, Pfefferle L. Simultaneous measurements of soot volume fraction and particle size/ microstructure in flames using a thermophoretic sampling technique. Combust Flame 1997;110(4):494–507. https://doi.org/10.1016/S0010-2180(97)00089-8.

[10] Leschowski M, Dreier T, Schulz C. An automated thermophoretic soot sampling device for laboratory-scale high-pressure flames. Rev Scientific Instrum 2014;85(4):045103https://doi.org/10.1063/1.4868970.

[11] Altenhoff M, Teige C, Storch M, Will S. Novel electric thermophoretic sampling device with highly repeatable characteristics. Rev Scientific Instrum 2016;87(12):125108https://doi.org/10.1063/1.4971988.

[12] Qiu L, Cheng X, Li Z, Wu H. Experimental and numerical investigation on soot volume fractions and number densities in non-smoking laminar n-heptane/n-butanol coflow flames. Combust Flame 2018;191:394–407. https://doi.org/10.1016/j.combustflame.2018.01.024.

[13] Li Z, Qiu L, Cheng X, Li Y, Wu H. The evolution of soot morphology and nanostructure in laminar diffusion flame of surrogate fuels for diesel. Fuel 2018;211:517–28. https://doi.org/10.1016/j.fuel.2017.09.036.

[14] Botero ML, Chen D, González-Calera S, Jefferson D, Kraft M. Hrtem evaluation of soot particles produced by the non-premixed combustion of liquid fuels. Carbon 2016;96:459–73. https://doi.org/10.1016/j.carbon.2015.09.077.

[15] Kashif M, Bonnety J, Matynia A, Costa PD, Legros G. Sooting propensities of some gasoline surrogate fuels: combined effects of fuel blending and air vitiation. Combust Flame 2015;162(5):1840–7. https://doi.org/10.1016/j.combustflame.2014.12.005.

[16] Botero ML, Mosbach S, Kraft M. Sooting tendency and particle size distributions of n-heptane/toluene mixtures burned in a wick-fed diffusion flame. Fuel 2016;169:111–9. https://doi.org/10.1016/j.fuel.2015.12.014.

[17] Dreyer JA, Poli M, Eaves NA, Botero ML, Akroyd J, Mosbach S, Kraft M. Evolution of the soot particle size distribution along the centreline of an n-heptane/toluene co-flow diffusion flame. Combust Flame 2019;209:256–66. https://doi.org/10.1016/j.combustflame.2019.08.002.

[18] Will S, Schraml S, Leipertz A. Two-dimensional soot-particle sizing by time-resolved laser-induced incandescence. Opt Lett 1995;20(22):2342–4. https://doi.org/10.1364/OL.20.002342.

[19] Bauer FJ, Daun KJ, Huber FJ, Will S. Can soot primary particle size distributions be determined using laser-induced incandescence? Appl Phys B 2019;125(6):109. https://doi.org/10.1007/s00340-019-7219-7.

[20] Hadef R, Geigle KP, Zerbs J, Sawchuk RA, Snelling DR. The concept of 2d gated imaging for particle sizing in a laminar diffusion flame. Appl Phys B 2013;112(3):395–408. https://doi.org/10.1007/s00340-013-5507-1.

[21] Tian B, Zhang C, Gao Y, Hochgreb S. Planar 2-color time-resolved laser-induced incandescence measurements of soot in a diffusion flame. Aerosol Sci Technol 2017;51(12):1345–53. https://doi.org/10.1080/02786826.2017.1366644.

[22] Schulz C, Kock B, Hofmann M, Michelsen H, Will S, Bougie B, Suntz R, Smallwood G. Laser-induced incandescence: recent trends and current questions. Appl Phys B 2006;83(3):333. https://doi.org/10.1007/s00340-006-2260-8.

[23] Michelsen H, Schulz C, Smallwood G, Will S. Laser-induced incandescence: particulate diagnostics for combustion, atmospheric, and industrial applications. Prog Energy Combust Sci 2015;51:2–48. https://doi.org/10.1016/j.pecs.2015.07.001.

[24] Liu F, Smallwood GJ, Snelling DR. Effects of primary particle diameter and aggregate size distribution on the temperature of soot particles heated by pulsed lasers. J Quant Spectrosc Radiative Transfer 2005;93(1):301–12. https://doi.org/10.1016/j.jqsrt.2004.08.027.

[25] Michelsen HA, Liu F, Kock B, Bladh H, Boiarciuc A, et al. Modeling laser-induced incandescence of soot: a summary and comparison of lii models. Appl Phys B 2007;87:503–21. https://doi.org/10.1007/s00340-007-2619-5.

[26] Goulay F, Schrader PE, López-Yglesias X, Michelsen HA. A data set for validation of models of laser-induced incandescence from soot: temporal profiles of lii signal and particle temperature. Appl Phys B 2013;112(3):287–306. https://doi.org/10.1007/s00340-013-5504-4.

[27] Liu F, Stagg BJ, Snelling DR, Smallwood GJ. Effects of primary soot particle size distribution on the temperature of soot particles heated by a nanosecond pulsed laser in an atmospheric laminar diffusion flame. Int J Heat Mass Transfer 2006;49(3):777–88. https://doi.org/10.1016/j.ijheatmasstransfer.2005.07.041.

[28] Lehre T, Jungfleisch B, Suntz R, Bockhorn H. Size distributions of nanoscaled particles and gas temperatures from time-resolved laser-induced-incandescence measurements. Appl Opt 2003;42:2021–30. https://doi.org/10.1364/AO.42.002021.

[29] Dankers S, Leipertz A. Determination of primary particle size distributions from time-resolved laser-induced incandescence measurements. Appl Opt 2004;43(18):3726–31. https://doi.org/10.1364/AO.43.003726.

[30] Snelling DR, Liu F, Smallwood GJ, Gülder Ömer L. Determination of the soot absorption function and thermal accommodation coefficient using low-fluence lii in a laminar coflow ethylene diffusion flame. Combust Flame 2004;136(1):180–90. https://doi.org/10.1016/j.combustflame.2003.09.013.

[31] Filippov A, Rosner D. Energy transfer between an aerosol particle and gas at high temperature ratios in the knudsen transition regime. Int J Heat Mass Transfer 2000;43(1):127–38. https://doi.org/10.1016/S0017-9310(99)00113-1.

[32] Melton LA. Soot diagnostics based on laser heating. Appl Opt 1984;23(13):2201–8. https://doi.org/10.1364/AO.23.002201.

[33] Liu F, Snelling DR, Thomson K, Smallwood GJ. Sensitivity and relative error analyses of soot temperature and volume fraction determined by two-color lii. Appl Phys B 2009;96:623–36. https://doi.org/10.1007/s00340-009-3560-6.

[34] Chang H, Charalampopoulos TT. Determination of the wavelength dependence of refractive indices of flame soot. Proc R Soc London A 1990;430(1880):577–91. https://doi.org/10.1098/rspa.1990.0107.

[35] Escudero F, Fuentes A, Consalvi J-L, Liu F, Demarco R. Unified behavior of soot production and radiative heat transfer in ethylene, propane and butane axisymmetric laminar diffusion flames at different oxygen indices. Fuel 2016;183:668–79. https://doi.org/10.1016/j.fuel.2016.06.126.

[36] Cortés D, Morán J, Liu F, Escudero F, Consalvi J-L, Fuentes A. Effect of fuels and oxygen indices on the morphology of soot generated in laminar coflow diffusion flames. Energy Fuels 2018;32(11):11802–13. https://doi.org/10.1021/acs.energyfuels.8b01301.

[37] Fuentes A, Henríquez R, Nmira F, Liu F, Consalvi J-L. Experimental and numerical study of the effects of the oxygen index on the radiation characteristics of laminar coflow diffusion flames. Combust Flame 2013;160(4):786–95. https://doi.org/10.1016/j.combustflame.2012.12.005.

[38] Pastor JV, García JM, Pastor JM, Buitrago JE. Analysis of calibration techniques for laser-induced incandescence measurements in flames. Meas Sci Technol 2006;17(12):3279–88. https://doi.org/10.1088/0957-0233/17/12/013.

[39] Desgroux P, Mercier X, Thomson KA. Study of the formation of soot and its precursors in flames using optical diagnostics. Proc Combust Inst 2013;34(1):1713–38. https://doi.org/10.1016/j.proci.2012.09.004.

[40] Goulay F, Schrader PE, Nemes L, Dansson MA, Michelsen HA. Photochemical interferences for laser-induced incandescence of flame-generated soot. Proc Combust Inst 2009;32(1):963–70. https://doi.org/10.1016/j.proci.2008.05.030.

[41] Kholghy MR, Afarin Y, Sediako AD, Barba J, Lapuerta M, Chu C, Weingarten J, Borshanpour B, Chernov V, Thomson MJ. Comparison of multiple diagnostic techniques to study soot formation and morphology in a diffusion flame. Combust Flame 2017;176:567–83. https://doi.org/10.1016/j.combustflame.2016.11.012.

[42] Dobbins RA, Megaridis CM. Morphology of flame-generated soot as determined by thermophoretic sampling. Langmuir 1987;3(2):254–9. https://doi.org/10.1021/la00074a019.

[43] Kholghy M, Saffaripour M, Yip C, Thomson MJ. The evolution of soot morphology in a laminar coflow diffusion flame of a surrogate for jet a-1. Combust Flame 2013;160(10):2119–30. https://doi.org/10.1016/j.combustflame.2013.04.008.

[44] Wang C, Chan QN, Zhang R, Kook S, Hawkes ER, Yeoh GH, Medwell PR. Automated determination of size and morphology information from soot transmission electron microscope (tem)-generated images. J Nanopart Res 2016;18(5):127. https://doi.org/10.1007/s11051-016-3434-x.

[45] Kempema NJ, Long MB. Combined optical and tem investigations for a detailed characterization of soot aggregate properties in a laminar coflow diffusion flame. Combust Flame 2016;164:373–85. https://doi.org/10.1016/j.combustflame.2015.12.001.

[46] Anderson PM, Guo H, Sunderland PB. Repeatability and reproducibility of tem soot primary particle size measurements and comparison of automated methods. J Aerosol Sci 2017;114:317–26. https://doi.org/10.1016/j.jaerosci.2017.10.002.

[47] Hu B, Koylu U. Size and morphology of soot particulates sampled from a turbulent nonpremixed acetylene flame. Aerosol Sci Technol 2004;38(10):1009–18. https://doi.org/10.1080/027868290519111.

[48] Vargas AM, Gülder Ömer L. Pressure dependence of primary soot particle size determined using thermophoretic sampling in laminar methane-air diffusion flames. Proc Combust Inst 2017;36(1):975–84. https://doi.org/10.1016/j.proci.2016.05.023.

[49] Wal RLV, Ticich TM, Stephens AB. Can soot primary particle size be determined using laser-induced incandescence? Combust Flame 1999;116(1):291–6. https://doi.org/10.1016/S0010-2180(98)00040-6.